Chemical routes to materials

Enhanced photoelectrocatalytic degradation of organic pollutants using TiO$_2$ nanotubes implanted with nitrogen ions

Xinggang Hou[1,*] , Xiaoli Liu[1], Jing Han[1], Huanli Liu[1], Jianghong Yao[2,*], Dejun Li[1], Liqun Wang[1], Bin Liao[3], Jing Li[1], and Ruijing Zhang[1]

[1] College of Physics and Materials Science, Tianjin Normal University, Tianjin 300387, China

[2] Key Laboratory of Weak-Light Nonlinear Photonics, Ministry of Education, TEDA Institute of Applied Physics and School of Physics, Nankai University, Tianjin 300457, China

[3] Key Laboratory of Beam Technology and Material Modification of Ministry of Education, College of Nuclear Science and Technology, Beijing Normal University, Beijing 100875, China

ABSTRACT

Nitrogen ions-implanted TiO$_2$ nanotubes (TNTs) were prepared by the methods of ion implantation and electrochemical anodic oxidation. The prepared samples were applied in photoelectrocatalytic (PEC) oxidation of methyl blue, rhodamine B and bisphenol A. Compared with pure TNTs, morphology, crystallinity, chemical structure, photoelectric and PEC ability of doped samples were greatly promoted because of ion implantation. The experimental results propose that the electronic structure of TiO$_2$ was modified because of the emergence of impurity states in the band gap by introducing nitrogen into the lattice, leading to the absorption of visible light. The synergy effects of tubular structures, doped nitrogen ions and the bias potential on the circuit are responsible for highly efficient and stable PEC activities induced by visible light and UV light. The doped TNTs prepared using the method of ion implantation could be applied to various areas, such as PEC water splitting and dye sensitized solar cells.

Introduction

Due to human activities, the water pollution arising from hazardous organic compounds is growing steadily around the world [1]. Those toxic pollutants cause serious environmental problems [1, 2]. To solve this environmental challenge, the technology of photocatalytic (PC) wastewater remediation has been given a great deal of attention because it is an effective method to deal with those recalcitrant organic pollutants [1–5]. TiO$_2$ is the most common photocatalyst for solving contamination problems on account of its environmentally friendly properties, such as

 Springer

low cost, nontoxicity, long durability and chemical stability [5, 6]. Among the various nanostructure of TiO_2 materials, well-ordered TiO_2 nanotube arrays (TNTs) prepared by the method of anodization have attracted extensive interest due to their tubular architecture providing larger surface area and significant lower photogenerated h^+–e^- pairs recombination rate than other nanostructured TiO_2 materials [7–11]. However, TiO_2 shows obvious PC activities excited by UV light only owing to its wide band gap (BG, 3.2 eV for anatase). In comparison with visible light (45%), UV light is merely a small fraction (5%) of the solar spectrum [12]. Therefore, numerous approaches have been applied to modify optical response of TiO_2 from UV to visible light range by reducing the threshold energy barrier, such as doping with some anions (C, S, F, B, P and N) [13–16]. So far, nitrogen-doped TiO_2 materials have been utilized in many PC applications [17–19]. It is convinced that the incorporation of nitrogen into the TiO_2 crystal lattice can easily take place due to characteristic features of small ionization energy and comparable size compared to oxygen atoms [18, 19]. The electronic and band structure of TiO_2 will be modified by introducing localized states at the top of the valence band (VB) on account of the doping of interstitial and substitutional nitrogen ions in the crystal lattice of TiO_2. As a result, the nitrogen-doped TiO_2 shows enhancement of PC activities under visible light irradiation due to reduced BG [2, 18].

From the beginning of the twenty-first century, the photoelectrocatalysis method, which is a combination of photocatalysis and electrochemistry, has attracted more and more attention [19–34]. In this method, an outer potential is biased on a semiconductor photoanode simultaneously when it is irradiated by light. The photogenerated electrons are migrated from the photoanode to the counter electrode through the outer circuit. The prevention of charge recombination can lead to the formation of higher amounts of holes. Then, more organic molecules of pollutants adsorbed on the photoanode surface are oxidized directly or destroyed indirectly by more quantities of •OH, which accelerate the mineralization of organic pollutants strongly in wastewater compared to classical photocatalysis. In the photoelectrocatalytic (PEC) process, the photoanode can be easily recycled for consecutive treatments and recovered after usage. Highly ordered TNTs are suitable for PEC applications very well. However, the large BG of TNTs still is

an obvious disadvantage in PEC applications. It is reported that the anodization in aqueous electrolyte of NH_4F and urea allowed nano-structuring and doping of nitrogen into TNTs simultaneously [35]. Therefore, doping nitrogen into TNTs to improve the PEC performance has become the preferred modification method due to those merits mentioned above.

So far, various methods have been applied to prepare nitrogen-doped TNTs including anodization in electrolyte containing nitrogen, anodization of a TiN alloy, heat treatment in NH_3 gas streams, wet immersion and annealing post-treatment, liquid phase deposition and ion implantation [35–40]. The properties of nitrogen-doped TiO_2, such as particulate morphology, BG, PC activities, doping sites and amounts, extremely depend on the synthetic method [41, 42]. It has been proposed in many studies that the lattice nitrogen atoms are beneficial to the visible light absorption, while several researchers attributed BG narrowing to NO_x and NH_x adsorbed on the surface [18, 42]. Thus, there is controversy about the dopant nature and electronic structure of nitrogen-doped TiO_2. As a typical engineering process, ion implantation is usually employed to modify the chemical and physical properties of semiconductor including TiO_2 [43–47]. Compared to other doping methods, the merits of ion implantation are that no any elements other than the interested one is involved, and a more reliable and much cleaner approach for introducing selected impurities into desired materials is offered. Nitrogen ions were introduced into TiO_2 films by the ion implantation in our previous work [48], and the bombardment of TNTs by this method with high energy (60 keV) was also reported [49]. However, the production of defects is a significant drawback of ion implantation, which mostly hinders the activation of the implanted ions [50]. Usually, the damage can be recovered by subsequent annealing process after ion implantation, which means two annealing procedures need to be done before and after implantation for implanted TiO_2 films or TNTs. We chose TNTs as the target of ion implantation at the start. However, when the TNTs were implanted using nitrogen ions with high energy (60 keV), highly ordered tubular structure of TNTs were severely destroyed (Fig. S1a). Even the ion energy was reduced to 10 keV, and the surface of TNTs was destructed seriously (Fig. S1b). So, the method of anodization of nitrogen-implanted Ti foils was chosen, in which the direct bombardment of

TNTs was avoided, and only one annealing procedure after ion implantation was made for crystallization.

The purpose of this work is to enhance the wastewater remediation ability of TNTs observably under both visible and UV light illuminations and clarify the mechanism of visible and UV light response of nitrogen-doped TNTs. Therefore, we proposed a novel method in which nitrogen ions were doped by ion implantation, and the wastewater remediation abilities of nitrogen-doped TNTs were evaluated by PEC degradation. Methyl blue (MB), rhodamine B (RhB) and bisphenol A (BPA) were chosen as dyes and chemical, respectively.

Experimental section

Materials

Titanium foils (0.25 mm thick, 99.9% purity) were purchased from Hebei Guowei Metal Material Limited Company. NH_4F (ammonium fluoride), ethylene glycol, ethanol, acetone, Na_2SO_4 (anhydrous sodium sulfate), MB, RhB, BPA, SOD (superoxide dismutase), EDTA (ethylenediaminetetraacetic acid) disodium salt dihydrate, t-BuOH ($tert$-butanol) were all of analytical grade purchased from Sigma-Aldrich. Deionized water was used throughout the work. All chemicals were used as received.

Preparation of nitrogen ions-implanted TNTs

Nitrogen ions were introduced into Ti foils with 60 keV ion energy and 10 mA/cm^2 current density using an implanter equipped with a Kaufman ion source. The chamber pressure prior to implantation was kept at a value as low as 10^{-4} Pa and then retaining the pressure at 10^{-2} Pa during ion implantation with a nitrogen flow rate of 6 sccm. The implanted doses were chosen as 1×10^{17}, 5×10^{17} and 1×10^{18} ions/cm^2. TNTs and nitrogen ions-doped TNTs were produced by the method of anodization using unimplanted and implanted Ti foils as anode, respectively. Before anodization, the Ti foils and nitrogen-implanted Ti foils were cleaned ultrasonically in alternate baths of acetone, ethanol and deionized water (10 min at each solvent) and then dried in air stream. During the anodization, a two-electrode system with platinum mesh as cathode and Ti foil and implanted Ti foils as anode was used at room temperature. The distance between the two electrodes was about 2 cm. The anodization was carried out in an electrolyte composed of ethylene glycol with 1 wt% water and 3 wt% NH_4F. The samples were anodized for 120 min with 50 V constant voltage using a DC power supply. Lastly, the anodized samples were dried in air (80 °C for 2 h) after being rinsed with deionized water and then were calcined at 450 °C for 4 h with heating rate of 5 °C min^{-1} in the ambient atmosphere. Those samples were marked as N-1-TNTs, N-5-TNTs and N-10-TNTs corresponding to the implanted TNTs with dose of 1×10^{17}, 5×10^{17} and 1×10^{18} ions/cm^2, respectively.

Characterization of TNTs and implanted TNTs

The morphologies of prepared samples were determined by field emission scanning electron microscope (FESEM, Hitachi SU8010) and transmission electron microscope (TEM, JEOL 2100F). The crystalline phases of the TNTs and implanted TNTs were analyzed by an X-ray diffractometer (XRD, X'Pert PRO MPD, PANalytical, Cu Kα radiation). The surface chemical composition of TNTs and nitrogen-implanted TNTs was identified using X-ray photoelectron spectroscopy (XPS, Shimadzu ESCA750) with Al Kα radiation. All the binding energies (BE) from XPS were referenced to the C 1s peak at 284.8 eV. The deconvoluted spectra of Ti 2p, O 1s and N 1s were made using Gaussian–Lorentzian peak fitting. The absorption spectra of those samples were recorded by a UV–Vis spectrometer (Shimadzu 3600) in the wavelength range of 250–700 nm.

The electrochemical impedance spectroscopy (EIS) of the TNTs and implanted TNTs was measured by an electrochemical workstation (CS350, CorrTest, China) at the room temperature. The Ag/AgCl electrode and platinum plate were used as reference electrode and counter electrode, respectively. The measurements were conducted in the frequency range of 10^5–0.01 Hz with amplitude of 5 mV in 0.1 M Na_2SO_4 solution at the open-circuit potential under the visible and UV light radiations. Mott–Schottky curves were measured at 1000 Hz.

PEC degradation measurements

The PEC degradation was performed in a cube quartz reactor (5 cm × 5 cm × 5 cm) containing 75 mL solution. The concentrations of MB, RhB and BPA used in the PEC degradation process were 80 mg L^{-1}, 80 mg L^{-1} and 50 mg L^{-1}, respectively. The TNTs and implanted TNTs were used as anodes, and a platinum mesh was used as cathode 1 cm away from anodes. The PEC measurements were conducted under 2 V bias potential provided by a DC voltage source (Dahua Instrument Corporation of Beijing). The supporting electrolyte was 0.1 M Na$_2$SO$_4$ solution. The tested solution was taken from the reactor periodically to analyze using UV-3600.

For the purpose of analyzing the main reactive radicals to oxidize MB, RhB and BPA in the PEC experiments, PEC degradations of MB, RhB and BPA with N-10-TNTs as anode were performed in the presence of three scavengers including 2 mM SOD (Superoxide Dismutase), 2 mM BuOH and 1 mM EDTA.

The wavelengths used as absorbance measurements were 664, 553 and 277 nm for MB, RhB and BPA, respectively. The removal efficiency of compound was examined according to the ratio of C_t and C_0, where C_t and C_0 are the absorbance of compound aqueous solution at time t and 0 at the analytical wavelength, respectively. The selected 365 nm UV light illumination was performed using a 500 W high-pressure mercury lamp. A 300 W tungsten–halogen lamp was chosen as the visible light source equipped with a cutoff filter with edge at 420 nm to remove UV light. The UV light intensity on the surface of samples was measured as 213 μW/cm^2 by an UV Irradiance Meter (UV-A, BNU), while the flux of the visible light was found to be 10,710 lx measured by an illumination photometer (ST-85, BNU).

Results and discussion

Characterization of nitrogen ions-implanted TNTs

Figure 1 shows the SEM and EDS images. The top view of TNTs and implanted TNTs are exhibited in Fig. 1a–d. All the nanotubes are vertically oriented with amount of small fragment on the surface which is the consequence of over corrosion during anodization. It should be noted that the average inner tube diameter of all the samples is in the range of 150–170 nm; therefore, the change in inner diameter of surface tube was not found with the same anodization conditions in the presence of different doses of implanted nitrogen ions. From the top views of the nanotubes, it can be found that the wall thickness increases with increasing doped nitrogen ions. The wall thickness of N-10-TNTs on the surface is in the range of 15–20 nm. It is apparent that the surface of all nitrogen ions-doped TNTs shows more orderly structure compared to TNTs, approving a better corrosion resistance of nitrogen ions-doped TNTs. Therefore, with the increase in the dose of implanted ions, well-organized tubular structure was obtained. A possible reason is that a dense nitrogen-doped nanolayer will be presented on the top of Ti foils after implantation. Thus, the increased corrosion resistance of the implanted samples was obtained, which leads to lower corrosion rate of nitrogen-implanted samples than pure Ti foils during anodization. As a result, implanted samples show more order tubular structure on the surface. Figure 1e, f is the typical cross section morphologies of TNTs and N-10-TNTs. Both TNTs and N-10-TNTs possess the same outer tube diameter which is identical to situation observed on the surface. Although top portion is broken partly, the tube structure of TNTs still can be detected. From the tube breakage of TNTs, the same wall thickness compared to surface is observed. However, N-10-TNTs has more compact structure compared to TNTs, and the wall thickness in the middle of the tube is estimated as 40 nm. The change in wall thickness from 15–20 nm (top of tube) to 40 nm (middle of tube) shows that the etching process on the top was milder than middle of tube for nitrogen-doped TNTs, which leads to increased wall thickness due to slow dissolution of side TiO$_2$. The existence of nitrogen was measured by EDS. Figure 1g, h is the evidence of the well-dispersed nitrogen element on the top of N-1-TNTs and N-10-TNTs. The results of EDS imply that a uniform distribution of nitrogen on the surface of TNTs has been attained using ion implantation method, and the content of nitrogen increases with the increase in dose of implantation. As shown in Fig. 1g, the tube structure is observed with a diameter about 160 nm for low dose of implantation, which is in agreement with SEM results.

Figure 1 Top views of SEM images of TNTs (**a**), N-1-TNTs (**b**), N-5-TNTs (**c**) and N-10-TNTs (**d**). Cross-sectional views of TNTs (**e**) and N-10-TNTs (**f**). EDS elemental mapping images of nitrogen of N-1-TNTs (**g**) and N-10-TNTs (**h**).

Characterization of nitrogen ions implanted TNTs
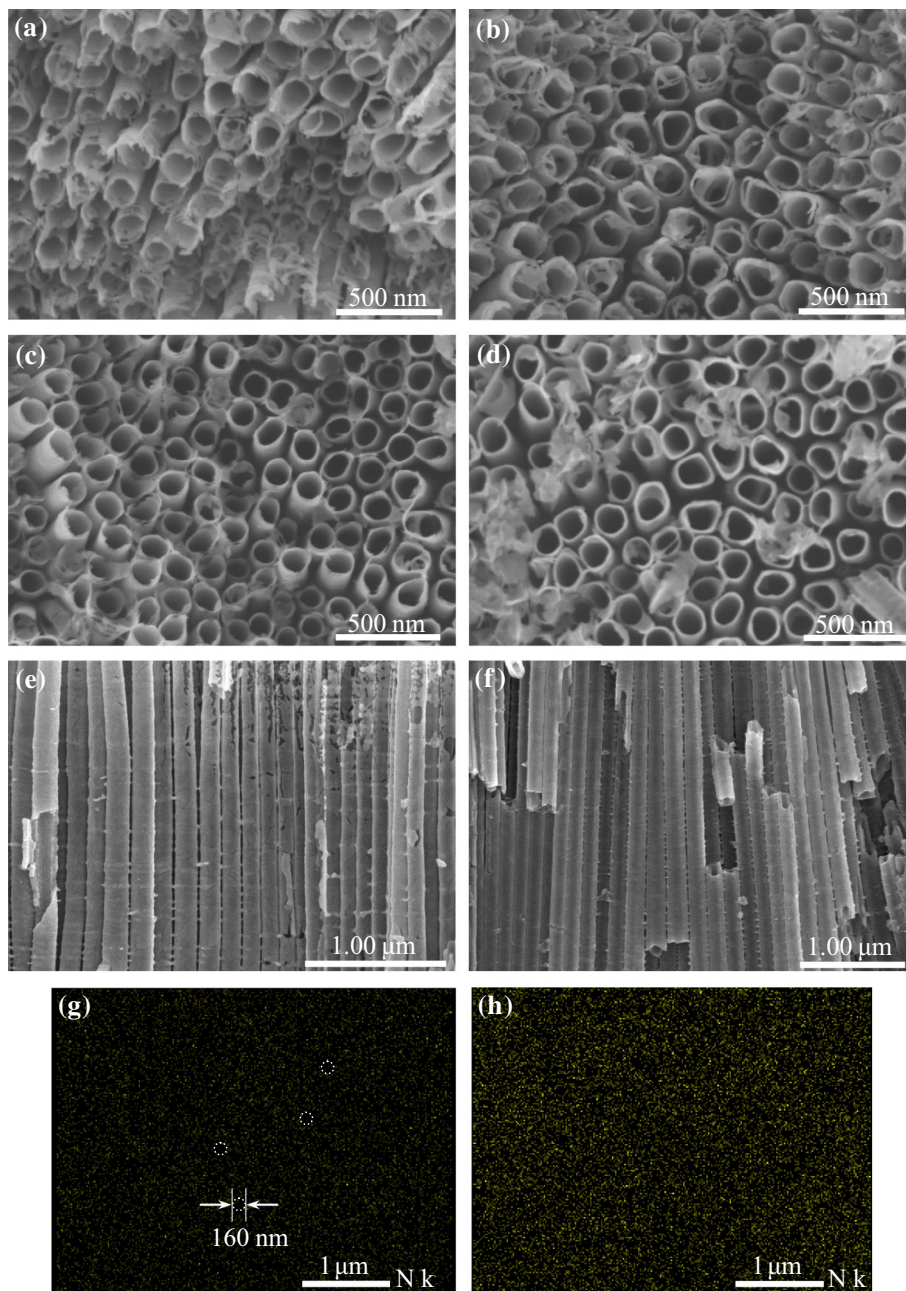
To show the tube structure of nitrogen ions-doped TNTs more clearly, high-resolution TEM (HRTEM) was used. A low-magnification HRTEM image of N-10-TNTs is presented in Fig. 2a, in which an ordered array tubular structure with uniform wall thickness is showed. Although the surface morphology of implanted TNTs was improved, the result confirms that ion implantation did not alter the tubular structure. Figure 2b–d is TEM images of single nanotube with higher magnification. From

Fig. 2b, it can be seen that the tube possesses wall thickness around 35 nm and diameter about 170 nm, which confirms the results observed from SEM. From Fig. 2b–d, it is also found some small bump attached to the straight walls of the nanotubes, which is not observed in SEM images. The crystalline structure of the nanotubes is confirmed in Fig. 2c, d, which was observed in the interior of nanotube, nanotube walls and small bump outside nanotubes. Three lattices spacing (*d*) of 0.237 nm, 0.247 nm and 0.352 nm are

Figure 2 TEM images of N-10-TNTs.
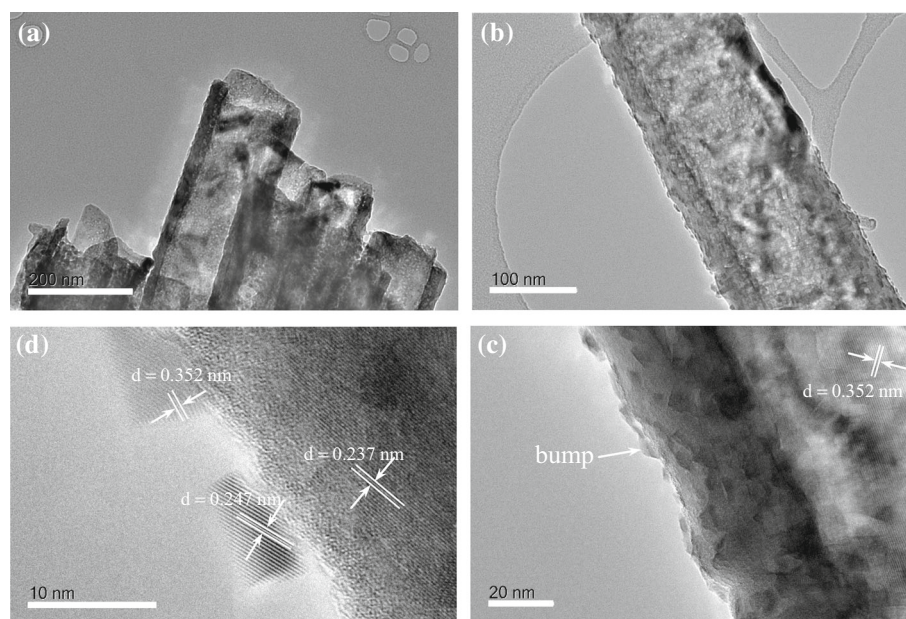
found, ascribed to the (004), (103) and (101) crystallographic planes of anatase phase TiO$_2$ available in the JCPDS#21-1272. The crystalline structure of interior of nanotube is plane (101) of anatase, while the nanotube walls is plane (103) of anatase. It is interesting that the crystalline structure of small bumps depends on the location, and two planes (004) and (101) corresponding to different bump are found in Fig. 2d.

XRD patterns of TNTs and nitrogen ions-doped TNTs are shown in Fig. 3a. The main characteristic peaks located at $2\theta = 25.3°$, $36.9°$, $37.9°$, $48.1°$, $54.0°$, $62.8°$, $70.6°$ and $76.2°$ are corresponding to (101), (103), (004), (200), (105), (204), (220) and (301) anatase phase TiO$_2$ crystallographic planes available in the JCPDS#21-1272, which shows that the dominant crystalline structure for all the samples is anatase phase. The doped nitrogen ions did not perturb the growth of anatase phase while annealing. For the purpose of estimating the effect of implantation on TiO$_2$ crystallite size, the average crystallites size (D) of TNTs and implanted TNTs was calculated from the anatase (101) diffraction data according to the Debye–Scherer formula ($D = \frac{0.9\lambda}{\Delta(2\theta)\cos\theta}$, where θ is the diffraction angle corresponding to the anatase (101) peak, $\Delta(2\theta)$ the width of half maximum of (101) peak, λ the used X-ray wavelength, and D the particle size in anatase (101) orientation). Therefore, the crystallite sizes decreased from $\sim$ 36 nm for TNTs down to $\sim$ 19 nm for N-10-TNTs. The nanocrystallites of this

scale are supposed to improve the PC activity of TiO$_2$ due to the increased surface area. For the nitrogen-doped TNTs, after ion implantation and annealing, no peaks corresponding to TiN crystal phase were observed, which is ascribed to uniform distribution of implanted nitrogen ions in the TiO$_2$ crystal lattice. Moreover, the samples N-5-TNTs and N-10-TNTs have more obvious peaks located at $27.5°$ and $36.0°$ corresponding to the (110) and (101) rutile phase TiO$_2$ crystallographic planes available in the JCPDS#65-1119, which represents that the temperature of anatase to rutile phase transition can be decreased after TNTs was doped with nitrogen [38]. This low-temperature transition can be understood as the instability of TiO$_2$ crystal structure after nitrogen doping due to reduced TiO$_2$ crystallite size and increased specific surface area. This mixed anatase and rutile crystal structure is beneficial to the PC activity. The Raman spectra are presented in Fig. 3b, in which typical anatase phase characteristics are exhibited. The Raman spectra confirm the anatase structure for the two samples which is in agreement to their XRD results. Usually, there are 10 optical phonons of symmetries in the anatase TiO$_2$, corresponding to $A_{1g} + A_{2u} + 2B_{1g} + B_{2u} + 3E_g + 2E_u$, in which the A_{1g}, $2B_{1g}$, B_{2u} and $3E_g$ are active in Raman spectra [40]. As shown in Fig. 3b, the Raman spectra of TNTs and N-10-TNTs have four characteristic peaks located at 146 (E_g), 396 (B_{1g}), 514 (B_{1g}/A_{1g}) and 641 (E_g) cm^{-1}. Raman lines from the anatase characteristic vibration

Figure 3 X-ray diffraction patterns of TNTs and nitrogen ions-doped TNTs with different dose (**a**), Raman spectra of TNTs and N-10-TNTs (**b**).
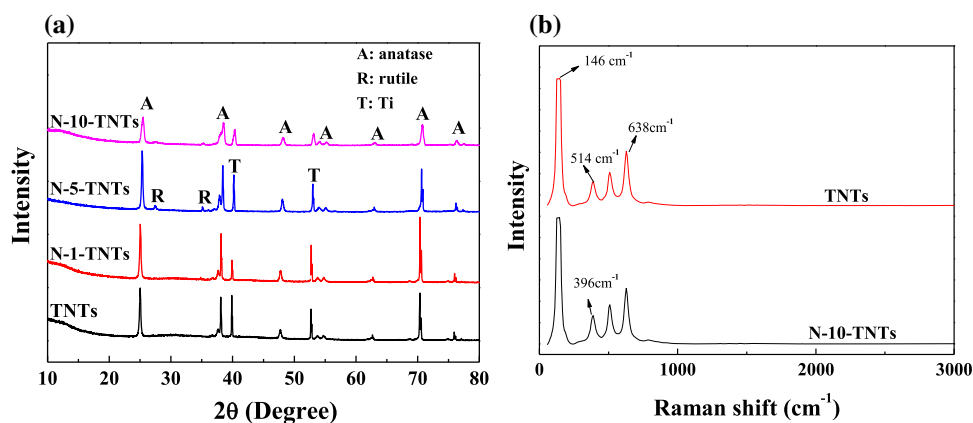

peak at 195 (E_g) and rutile phase have not been detected due to the weak signal. There is no significant difference in Raman spectra between TNTs and implanted TNTs.

As shown in Fig. 4, the chemical character and elemental composition of TNTs and implanted TNTs were analyzed by XPS. As shown in Fig. 4a, the surface nitrogen species were observed according to the N 1s XPS spectra of TNTs and implanted TNTs. The increased intensity of N 1s peaks corresponding to increased nitrogen content agrees with increasing of the dose of implantation. After being deconvoluted, the three sub-peaks located at 397.9, 399.1 and 400.7 eV can be attributed to the chemical bonding of N–Ti, N–O and N–N, which are ascribed to substitutional nitrogen, interstitial nitrogen dopant and molecularly chemisorbed nitrogen [35, 46]. Compared to the reported results, it is likely in this case that both Ti–N–O and Ti–O–N bonds are generated by introducing nitrogen and substitution of oxygen atoms in TiO_2 lattices after implantation and anodization treatment. After being analyzed, the area of the three sub-peaks, decreased substitutional N and increased interstitial N states were detected with increasing of the dose of implantation. However, the intensity of N 1s peak of N-10-TNTs is stronger than N-1-TNTs, which indicates that the absolute content of substitutional N in N-10-TNTs is much more than N-1-TNTs. In Fig. 4b, the doublet Ti $2p_{3/2}$ and Ti $2p_{1/2}$ (459.5 and 465.5 eV) is attributed to spin orbit-splitting, which is consistent with Ti^{4+} in TiO_2 lattice. After fitting, the peaks of N-1-TNTs and N-10-TNTs can be identified as Ti^{4+} ($2p_{3/2}$, 459.5 eV and $2p_{1/2}$, 465.6 eV) and Ti^{3+} ($2p_{3/2}$, 458.0 eV and $2p_{1/2}$, 464.7 eV), respectively [51]. The XPS results show the formation of the peak corresponding to Ti^{3+} for

implanted samples. The decrease in the peak area of Ti^{4+} together with increase in the peak area of Ti^{3+} was found with increasing dose of implantation, which can be used to estimate the change in stoichiometry of implanted TNTs. There are two possible reasons for the formation of Ti^{3+} and oxygen vacancies due to N doping. First, N doping induces a substantial reduction of the formation energy of Ti^{3+} and oxygen vacancies in TiO_2. Second, because of the lower electronegativity (3.04) and close radius of N ion (0.171 nm) compared to those of O ion (3.44, 0.140 nm), N ions incline to dope into the TiO_2 crystal lattice via substituting oxygen lattice positions resulting in partial electron transfer from N to Ti^{4+}, being accompanied by Ti^{3+} and oxygen vacancy formation [52, 53]. As shown in Fig. 4c, recorded O 1s spectra for all samples were separated into three chemical states. The state located at 530.7 eV binding energy (BE) can be assigned to oxygen belonging to TiO_2 crystal phase, while the state at BE of 531.8 eV is characteristic for surface TiO_x species and C=O, including the presence of Ti–O–N species for nitrogen-doped TNTs [35]. The last state located at BE of 532.8 eV can be ascribed to surface OH groups binding with surface atoms such as Ti–OH and C–OH [35]. As the analysis of peak of Ti 2p, the change in O stoichiometry can also be assessed by the change in relative peaks area. In the situation of nitrogen-doped TNTs, the peak area of 532.8 eV increases with increasing of the dose of implantation. The increased non-lattice oxygen area shows the generation of oxygen vacancies in TNTs lattice, which is in accordance with the XPS results of Ti 2p. It has been found that Ti^{3+}, oxygen vacancies, substitutional and interstitial nitrogen contribute to attain high PC activity and effective reduction of energy BG

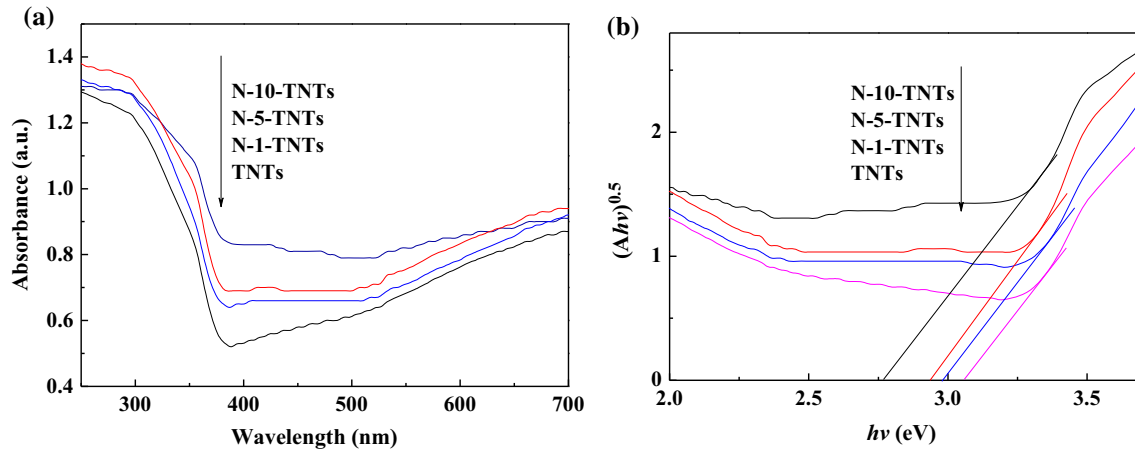**Figure 4** XPS spectra of TNTs and nitrogen ions-doped TNTs.
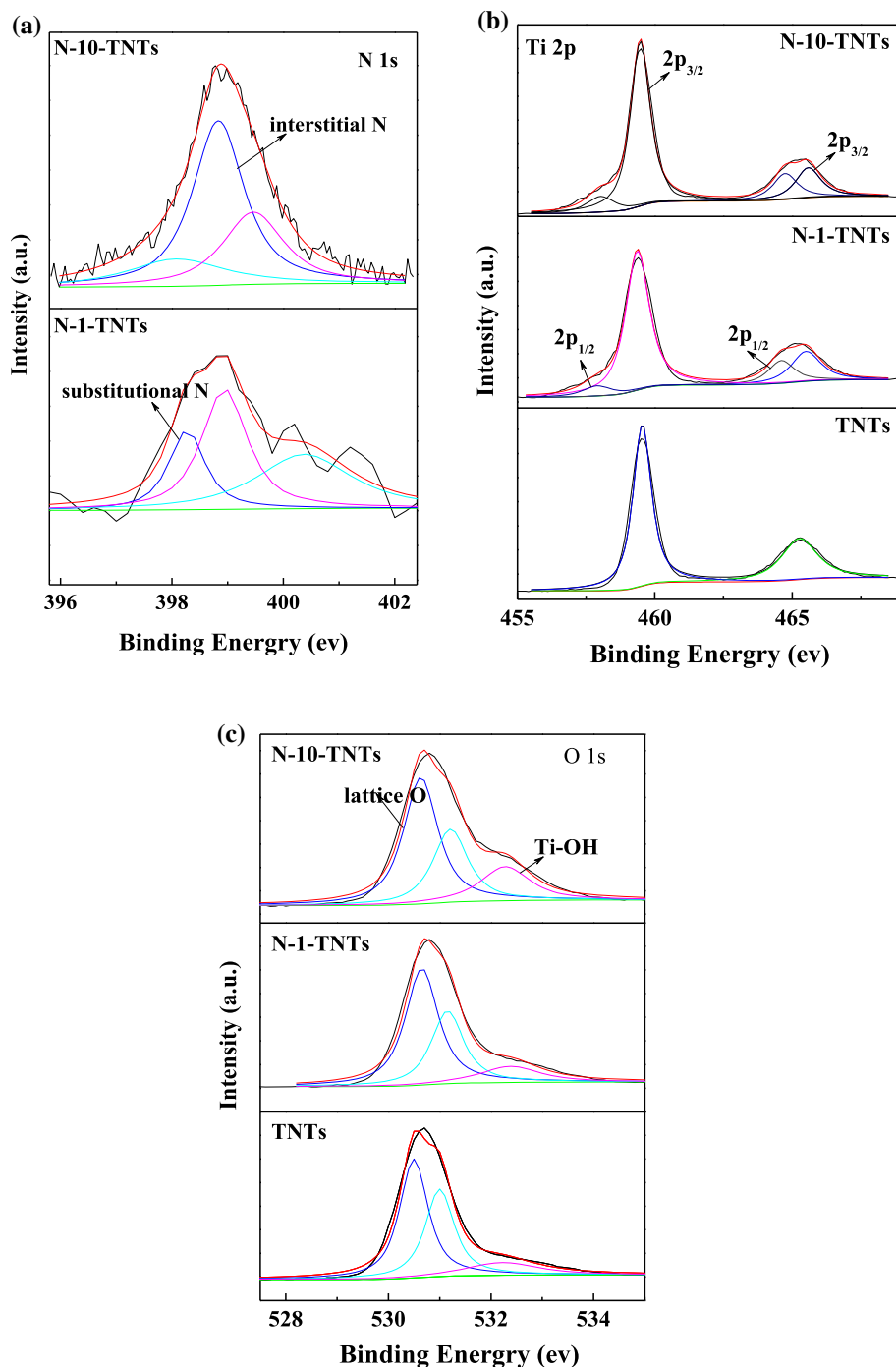
[2, 18, 51–53]. Therefore, higher PC activity is reasonable for the implanted TNTs.

Figure 5 shows the absorbance spectra for the samples and Tauc plots corresponding to the absorbance data. The BG of TNTs and implanted TNTs was determined using the formula $(hv\alpha)^{1/n} = A(hv - E_g)$ according to the procedure known as Tauc model [37], where E_g is BG, A is the proportional constant, h

is Plank's constant, v is the frequency of vibration, α is absorption coefficient and $n = 2$ due to indirect electron transition for anatase TiO_2. After $(hv\alpha)^{1/2}$ was plotted against hv using the function, a tangent line was drawn to intersect with horizontal axis, and then, the E_g value was obtained from the point of intersection. As shown in Fig. 5a, the absorbance spectra reveal a broad absorption in the range of 400–700 nm,

Figure 5 UV–Vis absorbance spectra of TNTs and nitrogen ions-doped TNTs.

which may be caused by impurity states, oxygen vacancies and Ti^{3+} states in the lattice of TNTs. The N-10-TNTs has the maximum absorption because dopant states reduce the BG. From Fig. 5b, it could be observed that nitrogen-doped TNTs display an obvious reduction in the BG. From the results, nitrogen doping reduces the BG of TNTs from 3.07 to 2.98 eV, 2.94 eV and 2.77 eV for N-1-TNTs, N-5-TNTs and N-10-TNTs, respectively, meaning that the corresponding absorption spectra were shifted from 404 nm to about 448 nm. The results clearly show that doped nitrogen, oxygen vacancies and Ti^{3+} states extended the absorption spectra of implanted samples to visible light region.

To explore the nature of interfacial behavior, the EIS measurements for TNTs and nitrogen-doped TNTs were performed. Figure 6a, b shows Nyquist plots when the TNTs and implanted TNTs were placed in electrolyte under visible and UV light irradiations. The corresponding Bode plots are presented in Fig. S2. Both Nyquist and Bode plots were understood by the equivalent circuit as shown in Fig. 6c. R_s corresponds to the solution resistance between the work and reference electrode. R_{tube} represents the resistance of tube layer paralleled with a constant phase element (CPE). R_{bar} and corresponding paralleled CPE denote the resistance and CPE of the barrier layer located at the bottom of the tube layer. The fitted parameters from the EIS data of the samples using ZView software are listed in Tables S1 and S2. According to Fig. 6a, b, all the Nyquist plots generally show a semicircle at high frequencies with an arc at low frequencies. The diameter of the observed semicircles is equal to the resistance of a charge transfer process. At high frequencies, the radius of the semicircle is not sensitive to both visible and UV light irradiations, which means similar R_s and R_{tube} for all the samples confirmed by the fitting data listed in Tables S1 and S2. At low frequencies, as shown in Fig. 6a, both nitrogen-doped TNTs show semicircle with smaller radius than the TNTs in the Nyquist plots and give R_{bar} values of 5351, 4532 and 3911 Ω cm^{-2} for the N-1-TNTs, N-5-TNTs and N-10-TNTs work electrode under visible light irradiation, which are far less than the value of the TNTs (39,194 Ω cm^{-2}). The phenomena is attributed to the new energy level in the BG created by oxygen vacancies, Ti^{3+} doping, substitutional and interstitial N, which contributes to the reduction of BG and improvement of the electron transfer rate, causing the higher PEC activity than that of the TNTs. However, the radius of the arc of both TNTs and nitrogen-doped TNTs decrease dramatically under UV light irradiation. The R_{bar} value of TNTs is reduced to 5559 Ω cm^{-2}, and the values are 5053, 4530 and 2539 Ω cm^{-2} for N-1-TNTs, N-5-TNTs and N-10-TNTs, respectively, which means that the combination of UV light and nitrogen doping can reduce the h^+–e^- pairs recombination rate and promote the charge transfer. From Bode and phase plots of the samples shown in Fig. S2, the PEC performance can be explained by the value of total resistance ($R_t = R_s + R_{tube} + R_{bar}$). The lowest R_t results in the highest PEC ability for N-10-TNTs compared with TNTs. The study of the lifetime τ_{el} of the photoexcited electrons in work electrode is investigated according to the Bode phase plot, which is deduced from equation $\tau_{el} = \frac{1}{2\pi f_{max}}$, where f_{max} is the
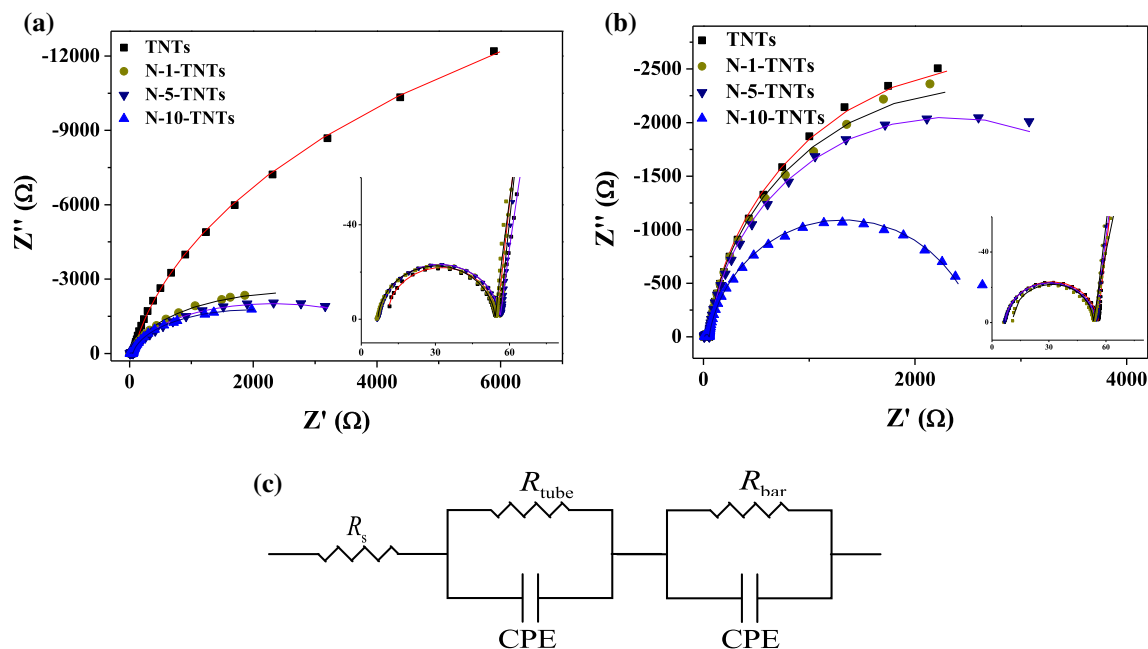
Figure 6 Nyquist plots of TNTs and nitrogen ions-implanted TNTs under light irradiation: visible (**a**), UV (**b**) and Model of equivalent circuit (**c**).

maximum frequency of the middle-frequency peak [54, 55]. From Fig. S2(b), the lifetime of electrons is calculated to be 0.23 ms, 1.18 ms, 1.48 ms and 1.48 ms for TNTS, N-1-TNTs, N-5-TNTs and N-10-TNTs, respectively, which exactly coincides with the order of their catalytic performance. These results represent that nitrogen doping increased τ_{el} of photoexcited electrons in work electrode by about a factor of 6.4 under visible light illumination. Longer lifetime for nitrogen-doped TNTs reveals effective separation of photogenerated charge carriers and better PC and PEC activities. However, the lifetime τ_{el} shows different rule when the samples were irradiated by UV light. The lifetime of electron is calculated to be 1.18 ms, 1.18 ms, 0.94 ms and 0.23 ms for TNTS, N-1-TNTs, N-5-TNTs and N-10-TNTs, respectively. However, it could be found that PEC activities of nitrogen-doped TNTs under UV light irradiation follow the order of N-10-TNTs > N-5-TNTs > N-1-TNTs > TNTs, which is contrary to the order of their lifetime. The performance shows that lifetime of nitrogen-doped TNTs under UV light irradiation for PEC activates is not important as under visible light irradiation. The possible reason will be continued to be discussed together with PEC degradation experiments in the section of PEC activities.

In order to find the flat band potentials and the majority carrier densities, Fig. 7 shows Mott–

Schottky plots of TNTs and nitrogen-doped TNTs, which was constructed according to the reciprocal of the square of capacitance ($1/C^2$) against applying potential. From the Mott–Schottky equation, the space charge capacitance C_{sc} of TNTs, and nitrogen-doped TNTs is described as: $C_{sc}^{-2} = \frac{2}{\varepsilon_0 \varepsilon e N_D}\left(U - U_{fb} - \frac{kT}{e}\right)$, where ε_0 is the dielectric permittivity of the vacuum, ε the dielectric constant of the semiconductor (100 for TNTs), e the elementary charge, N_D the donor density, k the Boltzmann constant, and T the temperature of the experiments (25 °C) [21, 37]. The flat band potential was acquired in accordance with the intercept to the horizontal axis of Mott–
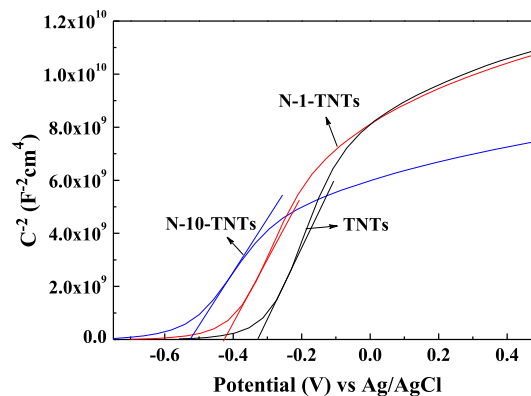
Figure 7 Mott–Schottky plots.

Schottky curves, which establishes the conduction band level of semiconductor with the reference of potential. The majority carrier density could be calculated by the slope. From Fig. 7, it could be seen that the nitrogen-doped TNTs have great difference in the donor density with the TNTs. Importantly, the nitrogen-doped TNTs show substantially smaller slopes compared to TNTs, revealing an increase in majority carrier densities due to nitrogen ion implantation. As mentioned above, flat band potentials could be estimated as -0.31 V, -0.41 V and -0.51 V for the TNTs, N-1-TNTs and N-10-TNTs, respectively, obtained from the Mott–Schottky curves. As shown in Fig. 7, the TNTs and nitrogen-doped TNTs indicate stronger charge capacitance dependence on the voltage. The positive slope of Mott–Schottky plots of TNTs and nitrogen-doped TNTs shows a n-type semiconductor behavior for the work electrode. From the curves, the majority carrier densities were calculated as 2.05×10^{19}, 3.64×10^{19} and 7.83×10^{19} cm^{-3} for TNTs, N-1-TNTs and N-10-TNTs. It is reasonable that the conductivity of nitrogen-implanted TNTs is enhanced. The increased majority carrier density can be attributed to the formation of substitutional and interstitial nitrogen state with a shallow donor for TNTs due to nitrogen ion implantation [46], which has been confirmed in the studies of XPS and UV–Vis spectra. Additionally, the increased band bending can be caused by the increased majority carrier densities at the surface of TNTs and then improve the charge separation in TNTs.

PEC activities

PEC degradation of MB, RhB and BPA

To discover the advantage of PEC degradation, the experiments for degradation of MB, RhB and BPA were performed under visible (Fig. 8a–c) and UV (Fig. 8d, e) light irradiation. The activities of PEC degradation of the samples were obtained with a duration of 80 min. The pseudo-first-order kinetics of MB, RhB and BPA degradation are shown in Fig. S3, and the obtained kinetic constant k is listed in Table 1. Furthermore, the time-dependent UV–Vis absorbance spectral of PEC degradation of MB, RhB and BPA for N-10-TNTs are shown in Fig. S4. The absorption peak of MB, RhB and BPA corresponding to 664, 553 and

277 nm decreased with increasing the time of irradiation, suggesting the organic compounds were decomposed into small molecules due to the attack by the active radicals. As shown in Fig. 8, the efficiency of PEC degradation increases with the dose-implanted ions. As shown in Fig. 8a, the MB removal rates of 40.6, 53.2, 55.5 and 65.3% within 80 min of the visible light irradiation are found for TNTs, N-1-TNTs, N-5-TNTs and N-10-TNTs, respectively. All the nitrogen-doped TNTs provide greater PEC degradation efficiency than that of TNTs. The N-10-TNTs result in the highest PEC MB degradation. The N-10-TNTs provide the highest rate constant value around 0.01386 min^{-1}, which is 1.3-, 1.4- and 2.7-fold of N-5-TNTs, N-1-TNTs and TNTs, respectively. The degradation efficiencies of RhB and BPA in the presence of the N-10-TNTs are shown in Fig. 8b, c. The PEC degraded RhB and BPA with efficiencies of 44.7 and 34.3% and rate constants of 0.00752 min^{-1} and 0.00456 min^{-1} for N-10-TNTs, respectively (Table 1). As shown in Fig. 8d–f, the PEC degradation of MB, RhB and BPA was performed in the presence of TNTs, N-1-TNTs, N-5-TNTs and N-10-TNTs under UV light irradiation. After 80 min, about 94.2, 57.9 and 47.1% of MB, RhB and BPA were removed by N-10-TNTs. The corresponding kinetic constants k for N-10-TNTs are up to 0.03515, 0.01132 and 0.00816 min^{-1}. The TNTs degraded 80.4, 43.2 and 33.3% of MB, RhB and BPA under same conditions.

The dyes and chemical molecules will first be adsorbed on the surface of TNTs and nitrogen-implanted TNTs and then experience the prominent PEC degradation. The PEC degradation has obvious superiority as the reaction proceed. By adding the helpful additional bias potential, the photogenerated electrons transfer from the working electrode to the counter electrode through the outer circuit. This will decrease the recombination rate and promote the separation of the photogenerated h$^+$–e$^-$ pairs. As a result, the quantity of photogenerated carriers increases greatly, which is beneficial to the creation of effective photoinduced charges. The increase in photogenerated carriers increases the number of active radicals and thus facilitates the PEC activity. So, more dyes and chemical can be degraded in the PEC process at the same time compared to PC degradation process. In addition, the photogenerated electrons separate and transfer quickly to the CB of TNTs in the level of femtosecond. Thus, the 0.23 ms lifetime provides enough transport time for the
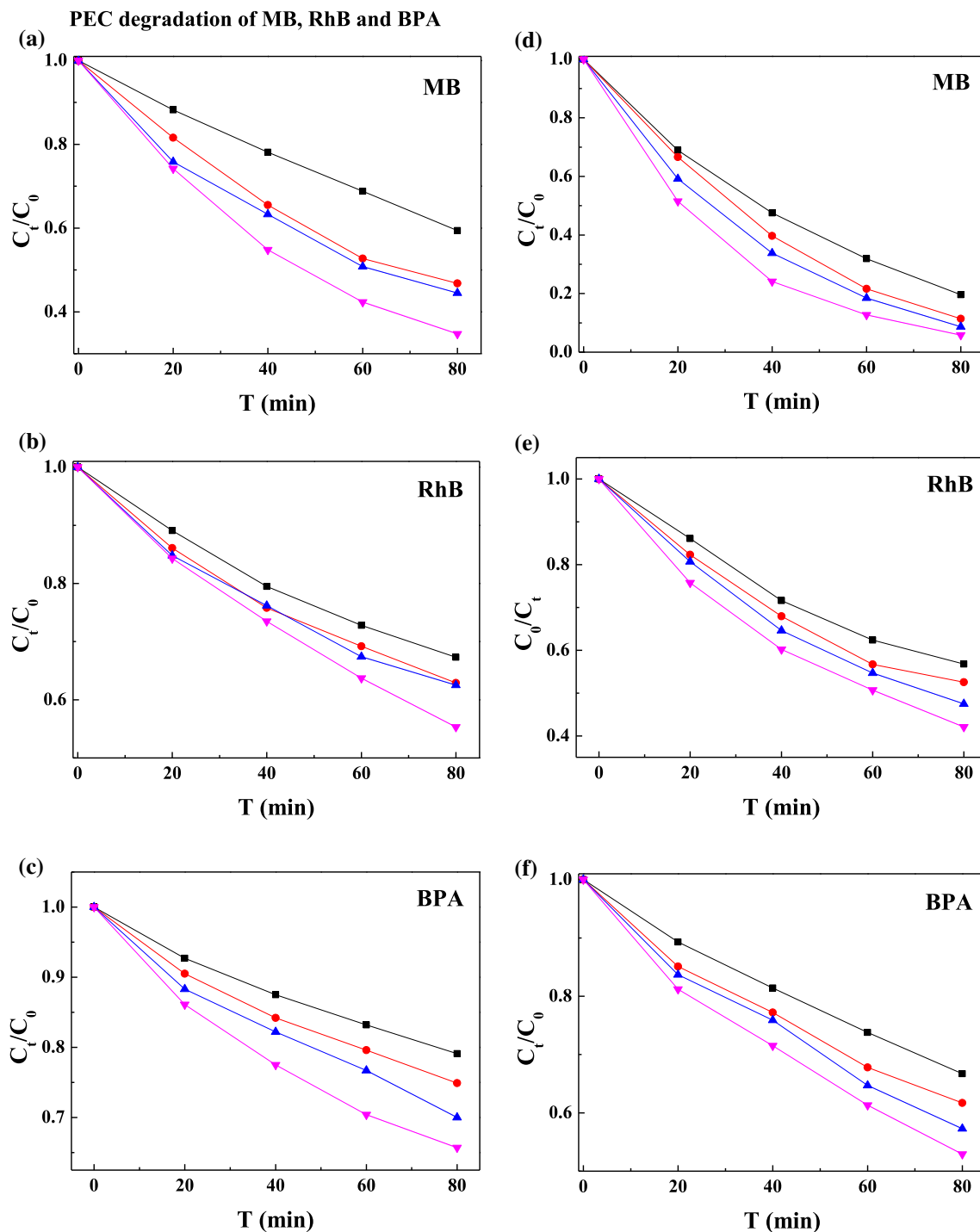
Figure 8 Comparison of PEC degradation rates for TNTs and nitrogen ions-implanted TNTs under light irradiation: **a–c** visible; **d–f** UV. Samples: ■ TNTs; ●N-1-TNTs; ▲N-5-TNTs; ▼N-10-TNTs.

carrier. From the Tables S1 and S2, the value of R_{bar} decreased with introducing of nitrogen ions into TNTs lattice. Concerning the fact that introducing nitrogen ions is more advantageous to the number and the separation of the photogenerated carriers

[37], the nitrogen-doped TNTs exhibit superior separation of photoinduced h^+–e^- pairs and faster transfer of photoinduced carriers than TNTs. It has been proved that electrons are easy to transfer into the underlying TiO_2 due to decreased R_{bar}; therefore,

Table 1 The PEC catalytic rate for the degradation of MB, RhB and BPA on the different samples

| | Pseudo-first rate constant (10^{-3} min^{-1}) | | | | | | | |
| | Visible light | | | | UV light | | | |
	TNTs	N-1-TNTs	N-5-TNTs	N-10-TNTs	TNTs	N-1-TNTs	N-5-TNTs	N-10-TNTs
MB	6.38 (± 0.07)	10.01 (± 0.28)	10.77 (± 0.41)	13.86 (± 0.35)	19.68 (± 0.38)	25.91 (± 0.86)	29.22 (± 0.74)	35.15 (± 0.32)
RhB	5.18 (± 0.15)	6.10 (± 0.23)	6.29 (± 0.26)	7.52 (± 0.11)	7.49 (± 0.24)	8.74 (± 0.37)	9.80 (± 0.29)	11.32 (± 0.39)
BPA	3.05 (± 0.10)	3.81 (± 0.05)	4.16 (± 0.31)	4.56 (± 0.17)	5.09 (± 0.05)	6.29 (± 0.19)	7.11 (± 0.18)	8.16 (± 0.22)

enhanced electrons injection and improved photo-application of TNTs will be found.

PEC degradation with various scavengers

To reveal the mechanism of PEC degradation further, the main active radicals during the decomposition of MB, RhB and BPA were distinguished through controlled experiments using SOD as scavenger for superoxide radicals, EDTA as holes scavenger and BuOH as hydroxyl radical scavenger [31]. From Fig. 9a, d, it can be seen that the addition of BuOH and EDTA led to rapid decrease for the degradation of MB. However, the PEC activity increased in the presence of SOD, which means that the •O^{2-} has no effect on the PEC degradation of MB. As displayed in Fig. 9b, e, it could be observed that the PEC degradation rate of RhB is in the order of SOD > EDTA > BuOH. It can be found that the •O^{2-} has small effect on the PEC degradation, while h$^+$ and •OH have far greater impact on it, which is in accordance with previous results [31]. As depicted in Fig. 9c, f, among the introduced scavengers, EDTA shows the highest restraining impact on the degradation of BPA. As for BuOH and SOD, SOD has greater PEC degradation rate than BuOH in removing BPA. The observations reveal h$^+$ and •O^{2-} are the major oxidant which is responsible for BPA degradation.

As known, the adsorbed oxygen molecules combine with scavenged electrons to form •O^{2-} on the surface of TNTs, which is restricted by the amount of unoccupied adsorption sites on surface of TNTs [56]. However, those adsorbed •O^{2-} can't be consumed as shown in Fig. 9a, d. Thus, those adsorbed •O^{2-} hinder degradation of MB further by decreasing of h$^+$

and •OH due to occupied active sites. After the addition of SOD, those adsorbed •O^{2-} are rapidly scavenged, which increase the surface activity of TNTs and then degradation rate of MB is accelerated. Because of the high chelating property, all the active sites on the surface of TNTs are occupied once EDTA is in the solution. As a result, the e$^-$–O or h$^+$–OH bonds aren't produced; therefore, no active radicals such as •OH or •O^{2-} are formed. Subsequently, the weakened PEC activity is observed because of the invalid h$^+$ and the lack of •O^{2-} which final product is still •OH [31]. However, the degradation of RhB and BPA was still valid in the presence of SOD and BuOH. The reason is that those scavengers capture the active radicals dispersed in solution while those adsorbed on the surface of N-10-TNTs survive; thus, adsorbed RhB and BPA molecules are oxidized. Besides, because SOD is specific for •O^{2-}, the •OH from h$^+$ and the surviving •O^{2-} on the surface of N-10-TNTs can still carry on in RhB and BPA removal.

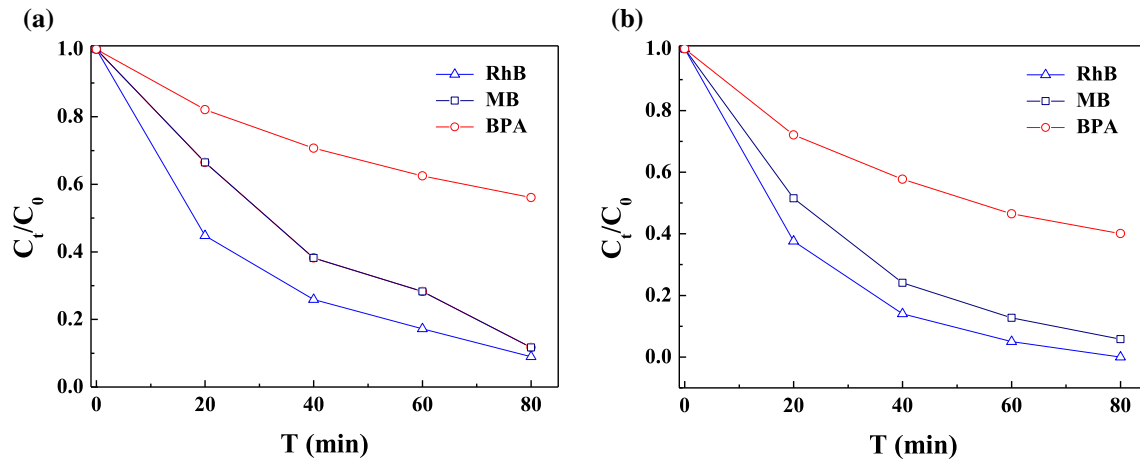## PEC degradation with different concentration

MB, RhB and BPA with lower concentration of 20 mg/L, 20 mg/L and 5 mg/L were also decomposed to research the effect of concentration on PEC degradation rate using N-10-TNTs under both visible and UV light illuminations. The results are shown in Fig. 10. After 80 min of visible light irradiation, 88.3%, 91.8%, and 43.9% of MB, RhB and BPA were decolorized, which show that the degradation rates were increased by 97.5%, 105% and 28.6%, respectively. When MB, RhB and BPA were irradiated by UV light, degradation rates were increased by 0.06%,
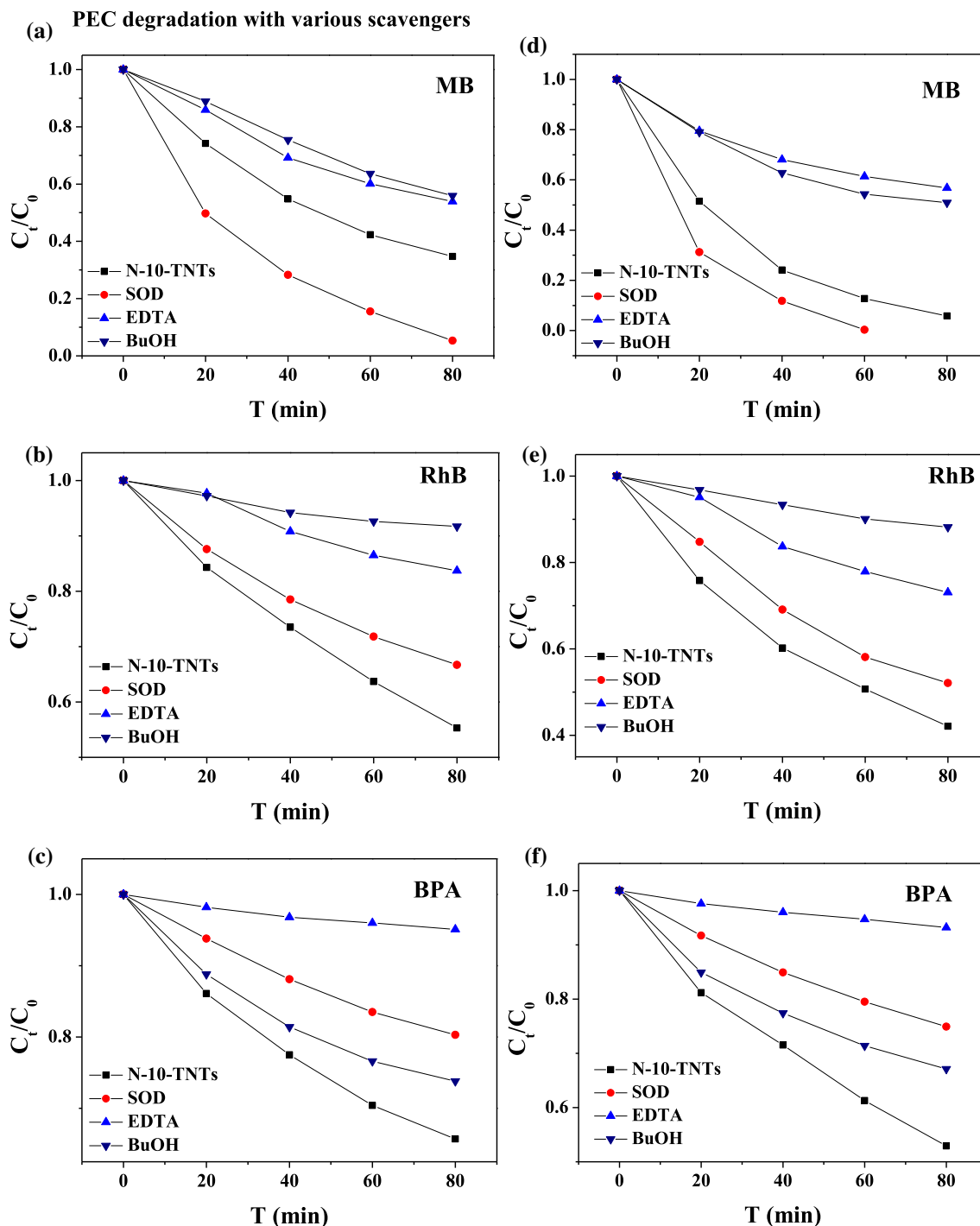
Figure 9 Effects of different scavengers on efficiencies of N-10-TNTs for PEC degradation of MB, RhB and BPA under visible (**a**–**c**) and UV light (**d**–**f**) irradiation.

72.7% and 27.1%, respectively. Among the three materials, PEC degradation of RhB and BPA is most affected under both visible and UV light illuminations. The efficiencies of RhB and BPA are found to be enhanced at a lower concentration. The PEC degradation of MB is remarkably improved under visible light irradiation only, which is the reason of high degradation rate at high concentration under UV light irradiation.

Figure 10 Effects of different concentration on efficiencies of N-10-TNTs for PEC degradation of MB, RhB and BPA under visible (**a**) and UV (**b**) light irradiation.

Possible PEC degradation mechanism

According to the experimental results mentioned above, the reasonable mechanism of PEC degradation of dyes and chemicals under visible and UV light irradiations is presented in Fig. 11. Because of formation of energy levels located above the VB edge due to nitrogen doping, the BG of TiO_2 in prepared nanotubes is narrowed. Moreover, these nitrogen levels are excellent traps for the Ti^{3+} electrons deriving from oxygen vacancies, which facilitate the creation of Ti^{3+} and oxygen vacancies to produce $\bullet O^{2-}$. Therefore, when nitrogen-doped TNTs are irradiated with visible light, the excited electrons will jump from the VB and nitrogen energy levels to the CB and impurity energy levels (associated with the presence of oxygen vacancies and Ti^{3+}), leaving holes in VB and nitrogen energy levels. Meanwhile, oxygen can be reduced to produce $\bullet O_2^-$ by photogenerated electrons, and $\bullet OH$ radicals can be generated by holes. These strong oxidizing radicals and holes could decompose dyes and chemical into macromolecules, CO_2 and H_2O on the surface of TNTs and nitrogen-doped TNTs in PEC degradation. While irradiating with UV light, electrons will be excited from both the VB and the nitrogen energy levels, and then, more holes are produced corresponding to higher photocatalytic efficiency than that under visible light illumination. Another probable mechanism for the efficient PEC degradation is that after photoexcited electrons transferring to the CB of TNTs, with the assistance from a small bias voltage applied to electrodes, the photogenerated electrons will migrate along the tube to metal substrate and finally reach the counter electrode through outer circuit. Then, the accumulated electrons located at counter electrode will reduce the absorbed oxygen molecules on this electrode further to form $\bullet O_2^-$. Subsequently, the activated $\bullet O_2^-$ can produce more $\bullet OH$ through a series of reactions with H^+, which is the reason of enhanced PEC degradation of dyes and chemical.

Conclusions

The PEC performance of nitrogen-doped TNTs synthesized by ion implantation was improved significantly under both visible and UV light irradiations. The experimental results indicate that impurities energy levels from Ti^{3+}, oxygen vacancies, nitrogen dopants are critical for PEC performance. We also confirmed that the superior activity of PEC process can be ascribed to the introduction of the bias potential, which reduces the transfer resistance of photoelectrons and accelerates the separation of h^+–e^- pairs. The TNTs photoelectrodes prepared using ion implantation and anodization show significant visible light- and UV light-induced PEC activity, which could open up exciting new opportunities in doping modification of TNTs, which is especially suitable for doping various nonmetal and metal ions into TNTs to improve PEC performance. This method also is able to combine with other methods to modify the PEC performance of TNTs, such as degradation of dyes and chemicals under optimum pH, deposition noble metal nanoparticles or semiconductor. These
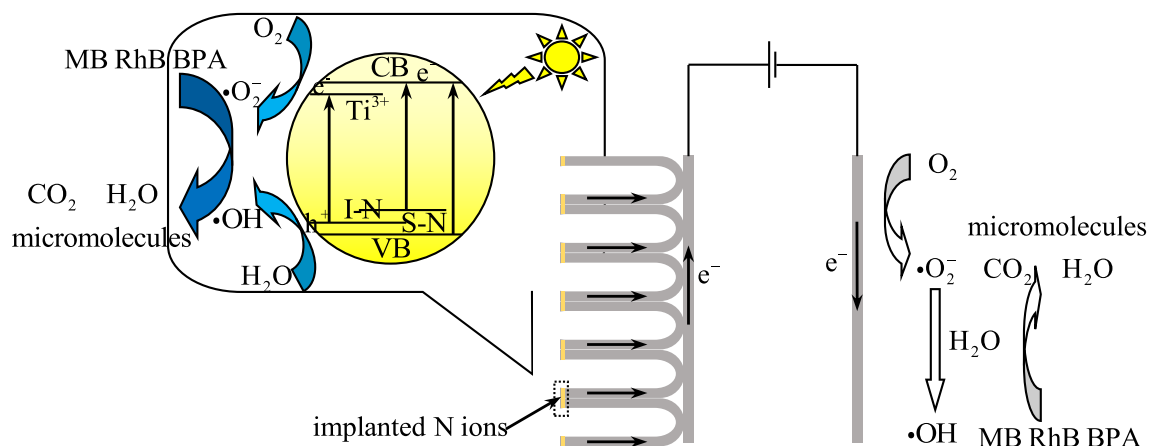
Figure 11 Schematic illustration of production and transfer of carriers during PEC degradation for nitrogen-doped TNTs under light irradiation.

results present a new sight for PEC degradation of organic compounds and are beneficial to understand the specific PEC degradation process.

Compliance with ethical standards

Conflict of interest No author has financial or other contractual agreements that might cause conflict of interest.

Electronic supplementary material: The online version of this article (https://doi.org/10.1007/s108 53-020-04461-5) contains supplementary material, which is available to authorized users.

References

[1] Keane DA, McGuigan KG, Ibáñez PF, Polo-López MI, Byrne AJ, Dunlop PSM, O'Shea K, Dionysiou DD, Pillai S (2014) Solar photocatalysis for water disinfection: materials and reactor design. Catal Sci Technol 4:1211–1226

[2] Fang W, Xing M, Zhang J (2017) Modifications on reduced titanium dioxide photocatalysts: a review. J Photochem Photobiol C 32:21–39

[3] Reddy PVL, Kim KH, Kavitha B, Kumar V, Raza N, Kalagara S (2018) Photocatalytic degradation of bisphenol A in aqueous media: a review. J Environ Manag 213:189–205

[4] Pelaez M, Nolan NT, Pillai SC, Seery MK, Falaras P, Kontos AG, Dunlop PSM, Hamilton JWJ, Byrne JA, O'Shea K, Entezari MH, Dionysiou DD (2012) A review on the visible light active titanium dioxide photocatalysts for environmental applications. Appl Catal B Environ 125:331–349

[5] Froschl T, Hormann U, Kubiak P, Kučerova G, Pfanzelt M, Weiss CK, Behm RJ, Hüsing N, Kaiser U, Landfester K, Wohlfahrt-Mehrens M (2012) High surface area crystalline titanium dioxide: potential and limits in electrochemical energy storage and catalysis. Chem Soc Rev 415:313–5360

[6] Fujishima A, Zhang XT, Tryk DA (2008) TiO$_2$ photocatalysis and related surface phenomena. Surf Sci Rep 63:515–582

[7] Ge MZ, Cao CY, Huang JY, Li SH, Zhang SN, Deng S, Li QS, Zhang KQ, Lai YK (2007) Synthesis, modification, and photo/photoelectrocatalytic degradation applications of TiO$_2$ nanotube arrays: a review. Nanotechnol Rev 5(1):75–112

[8] Regonini D, Bowen CR, Jaroenworaluck A, Stevens R (2013) A review of growth mechanism, structure and crystallinity of anodized TiO$_2$ nanotubes. Mater Sci Eng R 74:377–406

[9] Kowalski D, Kim D, Schmuki P (2013) TiO$_2$ nanotubes, nanochannels and mesosponge: self-organized formation and applications. Nano Today 8:235–264

[10] Lee K, Mazare A, Schmuki P (2014) One-dimensional titanium dioxide nanomaterials: nanotubes. Chem Rev 114:9385–9454

[11] Zubair M, Kim H, Razzaq A, Grimes CA, In S (2018) Solar spectrum photocatalytic conversion of CO$_2$ to CH$_4$ utilizing TiO$_2$ nanotube arrays embedded with graphene quantum dots. J CO2 Util 26:70–79

[12] Zhang Y, Cui WQ, An WJ, Liu L, Liang YH, Zhu YF (2018) Combination of photoelectrocatalysis and adsorption for removal of bisphenol A over TiO_2-graphene hydrogel with 3D network structure. Appl Catal B Environ 221:36–46

[13] Ji LJ, Zhang YH, Miao SY, Gong MD, Liu X (2017) In situ synthesis of carbon doped TiO_2 nanotubes with an enhanced photocatalytic performance under UV and visible light. Carbon 125:544–550

[14] Georgieva J, Valova E, Armyanov S, Tatchev D, Sotiropoulos S, Avramova I, Dimitrova N, Hubin A, Steenhaut O (2017) A simple preparation method and characterization of B and N co-doped TiO_2 nanotube arrays with enhanced photoelectrochemical performance. Appl Surf Sci 413:284–291

[15] Wang MY, Ioccozia J, Sun L, Lin CJ, Lin ZQ (2014) Inorganic-modified semiconductor TiO_2 nanotube arrays for photocatalysis. Energy Environ Sci 7:2182–2202

[16] Zaleska A (2008) Doped-TiO_2: a review. Recent Pat Eng 2:157–164

[17] Devi LG, Kavitha R (2014) Review on modified N-TiO_2 for green energy applications under UV/visible light: selected results and reaction mechanisms. RSC Adv 4:28265–28299

[18] Wang W, Tadé MO, Shao ZP (2018) Nitrogen-doped simple and complex oxides for photocatalysis: a review. Prog Mater Sci 92:33–63

[19] Etacheri V, Valentin CD, Schneider J, Bahnemann D, Pillai SC (2015) Visible-light activation of TiO_2 photocatalysts: advances in theory and experiments. J Photochem Photobiol C 25:1–29

[20] Garcia-Segura S, Brillas E (2017) Applied photoelectrocatalysis on the degradation of organic pollutants in wastewaters. J Photochem Photobiol C 31:1–35

[21] Xu Y, Ahmed R, Klein D, Cap S, Freedy K, McDonnell S, Zangari G (2019) Improving photo-oxidation activity of water by introducing Ti^{3+} in selfordered TiO_2 nanotube arrays treated with Ar/NH3. J Power Sources 414:242–249

[22] Zhang YZ, Xiong XY, Han Y, Zhang XH, Shen F, Deng SH, Xiao H, Yang XY, Yang G, Peng H (2012) Photoelectrocatalytic degradation of recalcitrant organic pollutants using TiO_2 film electrodes: an overview. Chemosphere 88:145–154

[23] Shen SH, Chen J, Wang M, Sheng X, Chen XG, Feng XJ, Mao SS (2018) Titanium dioxide nanostructures for photoelectrochemical applications. Prog Mater Sci 98:299–385

[24] Chatzitakis A, Papaderakis A, Karanasios N, Georgieva J, Pavlidou E, Litsardakis G, Poulios I, Sotiropoulos S (2017) Comparison of the photoelectrochemical performance of particulate and nanotube TiO_2 photoanodes. Catal Today 280:14–20

[25] Hua ZL, Dai ZY, Bai X, Ye ZF, Wang P, Gu HX, Huang X (2016) Copper nanoparticles sensitized TiO_2 nanotube arrays electrode with enhanced photoelectrocatalytic activity for diclofenac degradation. Chem Eng J 283:514–523

[26] Yao Y, Li K, Chen S, Jia JP, Wang YL, Wang HW (2012) Decolorization of Rhodamine B in a thin-film photoelectrocatalytic (PEC) reactor with slant-placed TiO_2 nanotubes electrode. Chem Eng J 187:29–35

[27] Liao WJ, Yang JW, Zhou H, Muruganathan M, Zhang YR (2014) Electrochemically self-doped TiO_2 nanotube arrays for efficient visible light photoelectrocatalytic degradation of contaminants. Electrochim Acta 136:310–317

[28] Li H, Xing JH, Xia ZB, Chen JQ (2014) Preparation of extremely smooth and boron-fluorine co-doped TiO_2 nanotube arrays with enhanced photoelectrochemical and photocatalytic performance. Electrochim Acta 139:331–336

[29] Suhadolnik L, Pohar A, Likozar B, Cěh M (2016) Mechanism and kinetics of phenol photocatalytic, electrocatalytic and photoelectrocatalytic degradation in a TiO_2-nanotube fixed-bed microreactor. Chem Eng J 303:292–301

[30] Wu J, Xu H, Yan W (2016) Photoelectrocatalytic degradation Rhodamine B over highly ordered TiO_2 nanotube arrays photoelectrode. Appl Surf Sci 386:1–13

[31] Yang LX, Li ZY, Jiang HM, Jiang WJ, Su RK, Luo SL, Luo Y (2016) Photoelectrocatalytic oxidation of bisphenol A over mesh of TiO_2/graphene/Cu_2O. Appl Catal B Environ 183:75–85

[32] Wu L, Li F, Xu YY, Zhang JW, Zhang DQ, Li GS, Li HX (2015) Plasmon-induced photoelectrocatalytic activity of Au nanoparticles enhanced TiO_2 nanotube arrays electrodes for environmental remediation. Appl Catal B Environ 164:217–224

[33] Xiang GL, Yu ZB, Hou YP, Chen Y, Peng ZB, Sun LF, Sun L (2016) Simulated solar-light induced photoelectrocatalytic degradation of bisphenol-A using Fe^{3+}-doped TiO_2 nanotube arrays as a photoanode with simultaneous aeration. Sep Purif Technol 161:144–151

[34] Zhou QX, Xing A, Li J, Zhao DC, Zhao KF, Lei M (2016) Synergistic enhancement in photoelectrocatalytic degradation of bisphenol A by CeO_2 and reduced graphene oxide co-modified TiO_2 nanotube arrays in combination with Fenton oxidation. Electrochim Acta 209:379–388

[35] Mazierski P, Nischk M, Gołkowska M, Lisowski W, Gazda M, Winiarski MJ, Klimczuk T, Zaleska-Medynska A (2016) Photocatalytic activity of nitrogen doped TiO_2 nanotubes prepared byanodic oxidation: the effect of applied voltage, anodization time and amount of nitrogen dopant. Appl Catal B Environ 196:77–88

[36] Xia L, Yang Y, Cao Y, Liu B, Lia XX, Chen XY, Song H, Zhang XM, Gao B, Fu JJ (2019) Porous N-doped TiO_2

nanotubes arrays by reverse oxidation of TiN and their visible-light photocatalytic activity. Surf Coat Technol 365:237–241

[37] Peighambardoust NS, Asl SK, Mohammadpour R, Asl SK (2018) Band-gap narrowing and electrochemical properties in N-doped and reduced anodic TiO$_2$ nanotube arrays. Electrochim Acta 270:245–255

[38] Yuan B, Wang Y, Bian HD, Shen TK, Wu YC, Chen Z (2013) Nitrogen doped TiO$_2$ nanotube arrays with high photoelectrochemical activity for photocatalytic applications. Appl Surf Sci 280:523–529

[39] Kodtharin N, Vongwatthaporn R, Nutariya J, Sricheewin C, Timah EN, Sivalertporn K, Thumthan O, Tipparach U (2018) Structures and properties of N-doped TiO$_2$ nanotubes arrays synthesized by the anodization method for hydrogen production. Mater Today Proc 5:14091–14098

[40] Souza JS, Krambrock K, Pinheiro MVB, Ando RA, Guha S, Alves WA (2014) Visible-light photocatalytic activity of NH$_4$NO$_3$ ion-exchanged nitrogen-doped titanate and TiO$_2$ nanotubes. J Mol Catal A Chem 394:48–56

[41] Bakar SA, Ribeiro C (2016) Nitrogen-doped titanium dioxide: An overview of material design and dimensionality effect over modern applications. J Photochem Photobiol C 27:1–29

[42] Lynch J, Giannini C, Cooper JK, Loiudice A, Sharp ID, Buonsanti R (2015) Substitutional or interstitial site-selective nitrogen doping in TiO$_2$ nanostructures. J Phys Chem C 119:7443–7452

[43] Rautray TR, Narayanan R, Kim K (2011) Ion implantation of titanium based biomaterials. Prog Mater Sci 56:1137–1177

[44] Elliman RG, Williams JS (2015) Advances in ion beam modification of semiconductors. Curr Opin Solid State Mater Sci 19:49–67

[45] Liu N, Häublein V, Zhou XM, Venkatesan U, Hartmann M, Mačković M, Nakajima T, Spiecker E, Osvet A, Frey L, Schmuki P (2015) "Black" TiO$_2$ nanotubes formed by high-energy proton implantation show noble-metal-*co*-catalyst free photocatalytic H$_2$-evolution. Nano Lett 15:6815–6820

[46] Wang GM, Xiao XH, Li WQ, Lin ZY, Zhao ZP, Chen C, Wang C, Li YJ, Huang XQ, Miao L, Jiang CZ, Huang Y, Duan XF (2015) Significantly enhanced visible light photoelectrochemical activity in TiO$_2$ nanowire arrays by nitrogen implantation. Nano Lett 15:4692–4698

[47] Han L, Xin YJ, Liu HL, Ma XX, Tang GZ (2010) Photo-electrocatalytic properties of nitrogen doped TiO$_2$/Ti photo-electrode prepared by plasma based ion implantation under visible light. J Hazard Mater 175:524–531

[48] Li J, Hou XG, Sun TT, Han J, Liu HL, Li DJ (2019) Hydrophilic, antibacterial and photocatalytic properties of TiO$_2$ composite films modified by the methods of N$^+$ ion implantation and doping of CNTs under visible light irradiation. Surf Coat Technol 365:123–128

[49] Zhou XM, Hublein V, Liu N, Nguyen NT, Zolnhofer EM, Tsuchiya H, Killian MS, Meyer K, Frey L, Schmuki P (2016) TiO$_2$ nanotubes: nitrogen-ion implantation at low dose provides noble-metal-free photocatalytic H$_2$-evolution activity. Angew Chem Int Ed 55:3763–3767

[50] Ronning C, Borschel C, Geburt S, Niepelt R (2010) Ion beam doping of semiconductor nanowires. Mater Sci Eng R 70(3–6):30–43

[51] Bharti B, Kumar S, Lee HN, Kumar R (2016) Formation of oxygen vacancies and Ti^{3+} state in TiO$_2$ thin film and enhanced optical properties by air plasma treatment. Sci Rep 6:32355

[52] Pan XY, Yang MQ, Fu XZ, Zhang N, Xu YJ (2013) Defective TiO$_2$ with oxygen vacancies: synthesis, properties and photocatalytic applications. Nanoscale 5:3601–3614

[53] Li HY, Zhang SL, Zhong Q (2013) Effect of nitrogen doping on oxygen vacancies of titanium dioxide supported vanadium pentoxide for ammonia-SCR reaction at low temperature. J Colloid Interface Sci 402:190–195

[54] Sun QN, Peng YP, Chen HL, Chang KL, Qiu YN, Lai SW (2016) Photoelectrochemical oxidation of ibuprofen via Cu$_2$O-doped TiO$_2$ nanotube arrays. J Hazard Mater 319:121–129

[55] Chen HL, Chen KF, Lai SW, Dang Z, Peng YP (2015) Photoelectrochemical oxidation of azo dye and generation of hydrogen via CN codoped TiO$_2$ nanotube arrays. Sep Purif Technol 146:143–153

[56] Ishibashi K, Fujishima A, Watanabe T, Hashimoto K (2000) Generation and deactivation processes of superoxide formed on TiO film illuminated by very weak UV light in air or water. J Phys Chem B 104(20):4934–5493